In situ ultrathin silica layer formation on polyamide thin-film composite membrane surface for enhanced forward osmosis performances

Nawshad Akther[a], Yuqing Lin[b], Shengyao Wang[b], Sherub Phuntsho[a], Qiang Fu[a], Noreddine Ghaffour[c], Hideto Matsuyama[b], and Ho Kyong Shon[a]*

[a] School of Civil and Environmental Engineering, University of Technology Sydney (UTS), NSW 2007, Australia

[b] Research Center for Membrane and Film Technology, Department of Chemical Science and Engineering, Kobe University, 1-1 Rokkodaicho, Nada-ku, Kobe 657-8501, Japan

[c] King Abdullah University of Science and Technology (KAUST), Water Desalination and Reuse Center (WDRC), Biological & Environmental Science & Engineering Division (BESE), Thuwal, 23955-6900, Saudi Arabia

[*] Corresponding author: Prof. Hokyong Shon Email: hokyong.shon-1@uts.edu.au; Tel.: +61 2 9514 2629; Fax: +61 2 9514 2633.

Abstract

Polyamide (PA) based thin-film composite (TFC) membranes experience a high degree of organic fouling due to their hydrophobic and rough membrane surfaces during forward osmosis (FO) process. In this study, an ultrathin silica layer was grown *in situ* on the PA surface to enhance the antifouling property of TFC membrane by silicification process. Surface characterization confirmed the development of a silica layer on the PA surface. The superhydrophilic surface of silica-deposited TFC membrane (contact angle of 20°) with 3 h silicification time (STFC-3h) displayed a 53% higher water flux than the pristine TFC membrane without significantly affecting the membrane selectivity. The silica-modified TFC FO membranes also exhibited excellent stability when subjected to long-term cross-flow shear stress rinsing using deionized (DI) water, including exposure to salty, acidic and basic solutions. Moreover, the fouling tests showed that STFC-3h membrane lost only 4.2%, 9.1% and 12.1% of its initial flux with bovine serum albumin (BSA), humic acid (HA) and sodium alginate (SA), respectively, which are considerably lower compared to the pristine TFC FO membrane where flux losses were 18.7%, 23.2% and 37.2%, respectively. The STFC-3h membrane also revealed higher flux recovery ratio (*FRR*) of 99.6%, 96.9% and 94.4% with BSA, HA and SA, respectively, after physical cleaning than the pristine membrane (91.4%, 88.7%, and 81.2%, respectively). Overall, the *in situ* formation of an ultrathin hydrophilic silica layer on the PA surface reported in this work shows that the TFC membrane's water flux and antifouling property could be improved without diminishing the membrane selectivity.

Keywords: Forward osmosis (FO); Thin-film composite (TFC); Polyamide membrane; Surface modification; Silica nanoparticles

1 Introduction

Osmotically-driven membrane processes like forward osmosis (FO) have been widely studied in recent decades for wastewater treatment [1], wastewater reclamation and seawater dilution [2], resource recovery [3], and food processing [4] due to their high water recovery, reduced fouling tendency and low energy consumption as opposed to pressure-driven membrane processes like reverse osmosis (RO). FO processes are driven by the osmotic pressure gradient existing between the high salinity draw solution (DS) and low salinity feed solution (FS) streams across the semipermeable membrane [5, 6]. As a result, FO processes are considered to be more energy-efficient than RO when used in applications that do not require DS recovery.

State-of-the-art aromatic polyamide (PA) thin-film composite (TFC) membranes have been considered promising candidates for various separation processes due to their high degree of tunability, unparalleled permeability-rejection performance, and broader pH tolerance range in comparison to the cellulose-based membranes [7, 8]. The PA TFC membrane consists of a PA selective layer formed via interfacial polymerization (IP) reaction on top of a mechanically robust porous substrate [9]. Despite being considered the benchmark for water treatment membranes, the PA TFC membranes experience the trade-off between water permeability and draw solute selectivity. Additionally, the characteristic rough and hydrophobic surface of the PA selective layer increases the membrane fouling propensity, which in turn severely hinders the treatment of high-fouling wastewaters. Consequently, the deteriorated membrane performance escalates the overall process energy requirement, operational costs, and reduces membrane life. Therefore, it is imperative to design the structural and chemical properties of FO membranes to prevent or reduce foulant build-up on the membrane surface, while retaining a high membrane separation performance.

Membrane surface properties, such as high hydrophilicity and low roughness, have demonstrated to play an essential role in enhancing the antifouling properties of membranes by

limiting their affinity to interact with the organic matter; thereby, reducing physisorption of foulants [10]. To diminish the fouling of PA TFC membranes, researchers have developed various methods, such as rendering the PA layer surface smoother, making membrane surface more hydrophilic and less charged through alteration of the IP process[11], plasma surface treatment [12], hydrophilic macromolecule attachment via dip-coating [13], and free radical [14] or graft polymerizations [15]. Nonetheless, the use of the above techniques is not very useful because their scope for enhancing fouling control is limited. Other strategies include embedding nanomaterials within the PA selective layer [16-18] or coating them on the PA surface to modify the membrane properties [19]. For instance, it has been observed that when nanomaterials like carbon nanotubes [20], halloysite nanotubes [21], graphene oxide [22-24], covalent organic frameworks [16, 17] and silver nanoparticles [25] are incorporated into the PA selective layer, the antifouling properties of thin-film nanocomposite (TFN) membranes can be improved. However, such modification methods can influence the membrane separation performance by affecting the chemical properties of the PA layer, and result in inadequate use of the nanomaterial surface as most of it is embedded in the polymer matrix.

On the contrary, coating the nanoparticles on the PA layer via grafting, covalent bonding, surface mineralization or layer-by-layer (LbL) assembly methods is more desirable for tuning membrane performance, hydrophilicity, surface roughness and charge to improve chlorine resistance, delay membrane fouling and provide biocidal properties without considerably varying the intrinsic membrane structures [26]. For example, Tiraferri et al. imparted biocidal properties to the TFC membrane surface by binding CNTs to the PA surface using amide bonds, which inactivated up to 60% of the bacteria attached to the membrane within one hour [7]. Hegab et al. covalently attached antibacterial GO sheets to the TFC membrane surface using hybrid and layer-by-layer (LbL) grafting techniques [27]. Yu's group, on the other hand, improved the fouling resistance and water flux recovery of the membrane by applying surface

mineralization technique to uniformly deposit silver chloride on membrane surface via an alternate soaking process (ASP); where the mineralization degree was controlled by varying the number of ASP cycles [28]. Atomic layer deposition (ALD) coating using trimethylaluminum was also explored to alter the TFC membrane surface for better antifouling performance [29]. Although nanomaterial coating methods have been extensively utilized to boost the membrane surface properties and antifouling performance, the above techniques are sophisticated because they require large quantities of chemicals, and involve several complicated treatment steps/cycles with exceptionally challenging operating conditions, which limit their scalability. In addition, physical surface coating methods may result in leaching or detachment of nanoparticles from the membrane surface, which would reduce membrane functionality and induce secondary environmental pollution (e.g. leaching of toxic silver ions) [30]. Moreover, uncontrolled and thick deposition of nanoparticles on the membrane surface could increase mass transfer resistance and reduce water flux across the membrane. Therefore, ultrathin coating layers on the membrane surface with good chemical and mechanical stability are preferable to reduce the water transport resistance and prevent leaching of nanomaterials from the membrane surface.

Silica nanoparticles have been previously used for surface modification due to their hydrophilicity, widespread availability and low cost [31-36]. For instance, Huang et al. grafted amine-functionalized silica nanoparticles on the nanofiltration membrane surface to augment its hydrophilicity and antifouling properties [37]. Zhang et al. created a superhydrophilic interface structure by growing a silica layer on the polyketone substrate for treating challenging oily emulsions [35]. The silica-modified membranes demonstrated exceptional antifouling properies against a variety of oily emulsions comprising of several pollutants like natural organic materials, surfactants and proteins; and achieved a flux recovery ratio (*FRR*) of nearly 100% after several cycles of oily emulsion filtration.

In this study, we developed TFC FO membrane modified with an ultrathin silica layer on the PA surface via *in situ* silicification process. The silicification process was initiated using 3-aminopropyltriethoxysilane (APTES) and tetraethoxysilane (TEOS) as the silane coupling agent and silica precursor, respectively. The influence of silicification time on the membrane surface properties, morphology and performances was systematically examined. The silica-coated PA TFC membrane demonstrated a hydrophilic surface with improved antifouling properties. Additionally, the silicification method used in this study is comparatively facile, efficient and straightforward compared to other surface modification techniques, such as LbL and ALD. Unlike the polymer or hydrogel coatings on the membrane surface that increase the water transport resistance across the membrane [38], the ultrathin silica layer significantly improved the membrane's surface hydrophilicity and water permeability without adversely affecting its selectivity. Moreover, the silica layer on the TFC membrane surface demonstrated excellent stability to long-term stress from deionized (DI) water cross-flow rinsing, in addition to improved fouling resistance to organic foulants. Consequently, this facile membrane surface modification method can deliver valuable insights into the design and preparation of antifouling PA TFC FO membranes.

2 Experimental method

2.1 Materials

Solvay supplied polysulfone pellets (PSf, Udel® P-3500). M-phenylenediamine flakes (MPD, 95%), 1-methyl-2 pyrrolidone (NMP, super dehydrated), n-hexane (96%), sodium chloride (NaCl, 99.5%), calcium chloride ($CaCl_2$, 90%), ethanol (EtOH, 99.5%), bovine serum albumin (BSA, fraction V), and ammonia (25%) were procured from FUJIFILM Wako Pure Chemical Corporation and used without further purification. Tetraethoxysilane (TEOS, >97%), 1,3,5-benzenetricarbonyl trichloride (TMC, >98%), 3-aminopropyl-triethoxysilane (APTES, >98%)

were bought from Tokyo Chemical Industry and employed as received. Humic acid (HA) sodium salt and sodium alginate (SA, 300 cps) were supplied by Nacalai Tesque, Inc. and Sigma Aldrich, respectively. DI (~18 MΩ.cm^{-1}, Milli-Q®, Merck) was used to make DS and FS.

2.2 Membrane fabrication

The porous PSf flat sheet substrates were prepared from 12 wt% PSf dope solution using the non-solvent induced phase separation (NIPS) technique, as described in our previous work [16]. More details are provided in the Supplementary Information (SI). TFC membranes were prepared by forming PA selective layers on the PSf substrate surfaces through IP reaction. First, the substrate was immersed in a 4 wt% MPD aqueous solution for 2.5 min, and the excess solution was removed using filter paper. The amine-saturated substrate was then exposed to 0.1 wt% TMC/n-hexane organic solution for 1 min to initiate the IP reaction, followed by heat treatment for 5 min at 60 °C to improve the PA cross-linking degree. The prepared TFC membranes were stored in DI water at 4 °C prior to surface modification. More information is provided in the SI.

2.3 Membrane surface modification

The APTES decoration and *in situ* silicification process on the membrane surfaces were conducted using the protocols from our previous work [35]. In short, the TFC membrane was first dipped in a 2 wt% APTES solution for 16 h to endow positive charge to the PA layer. The APTES-decorated TFC membrane was denoted as 'APTES-TFC'. A mineral precursor solution prepared by mixing 100 mL EtOH, 4 mL ammonia and 1.5 mL TEOS for 5 min was then immediately contacted with the PA layer of the APTES-TFC membrane for various durations (1, 3 and 5 h) to start the *in situ* silicification process. The resultant silica-coated TFC membranes were denoted as 'STFC-1h', 'STFC-3h' and 'STFC-5h' depending on the

silicification time. The modified membranes were gently rinsed by shaking in DI water at 50 rpm for 24 h to remove any loose silica particles. The resultant membranes were then kept in DI water at 4 ºC until use.

2.4 Membrane characterization

The PA layer and cross-sectional morphologies of all the membranes were examined using field emission scanning electron microscopy (FESEM; JEOL) with a 10 mA emission current and 5 kV accelerating voltage. Osmium plasma coating was applied to the samples before SEM analysis to obtain a conductive thin film. Atomic force microscopy (AFM; SPI3800 N/SPA 400, Seiko Instruments Inc.) was used in non-contact mode to measure the membrane surface roughness for a scan area of 5 μm × 5 μm. The surface chemical compositions of the membranes were studied by X-ray photoelectron spectroscopy (XPS; JSP-9010MC, JEOL) with an Al-Kα radiation source (1486.6 eV), Fourier-transform infrared spectroscopy with attenuated total reflectance (FTIR-ATR; Bruker), and energy-dispersive X-ray spectroscopy (EDS) with an emission current and accelerating voltage of 25 mA and 12 kV, respectively.

The membrane surface hydrophilicity was determined from the water contact angles measured on at least 5 random positions for each sample with a contact angle goniometer (Drop Master 300, Kyowa Interface Science Co.) at room temperature. An electro-kinetic analyzer (SurPASS™ 3, Anton Paar) was utilized to verify the membrane surface charge by measuring the zeta potential of the membranes. The zeta potential tests were conducted at a gap height of 100 μm with 1 mM KCl electrolyte solution, and its pH was adjusted between 3 and 10 by dosing with 0.05 M HCl and NaOH solutions.

2.5 Membrane performance assessment

2.5.1 FO performance

A laboratory-scale FO experimental setup was utilized to establish the membrane performance with an effective surface area of 4.5 cm^2. The FO cell comprised of a 2.5 mm deep spacer-free flow channel on either side of the membrane. A co-current flow rate of 250 $mL.min^{-1}$ at 22 °C was used for both the DS and FS during the FO tests. The membranes were examined in AL-FS (active layer facing to FS) mode with DI water and 1 M NaCl as FS and DS, respectively. The water flux (J_w, $L.m^{-2}.h^{-1}$) and the reverse solute flux (J_s, $g.m^{-2}.h^{-1}$) through the membrane were determined from Eqs. (S1) and (S2), respectively. The specific reverse solute flux (*SRSF*, $g.L^{-1}$) was evaluated from J_w and J_s values to specify the membrane selectivity (Eq. (S3)). The equations utilized for assessing the membrane performance are included in the SI.

2.5.2 Membrane intrinsic transport parameters

The intrinsic membrane transport parameters were obtained using a cross-flow laboratory-scale RO filtration system with an active membrane area of 7.06 cm^2. All membrane samples were pre-compacted with DI water at 6 bar for 1 h at a flow rate of 9.9 $mL.min^{-1}$ before testing to obtain a stable flux. The pressure was then reduced to 5 bar to obtain the pure water flux (J) and water permeability coefficient (A, $L.m^{-2}.h^{-1}.bar^{-1}$) using Eqs. (1) and (2), respectively.

$$J = \frac{\Delta V}{A_m . \Delta t} \tag{1}$$

$$A = \frac{J}{\Delta P} \tag{2}$$

where (ΔV, L), (A_m, m^2), (Δt, h) and (ΔP, bar) are the permeate volume, effective membrane surface area, filtration duration and applied pressure difference, respectively.

The DI water feed was then replaced by 10 mM NaCl solution at 5 bar to determine the solute rejection (R, %) and solute permeability coefficient (B, L.m^{-2}.h^{-1}) using Eqs. (3) and (4), respectively:

$$R = \left(1 - \frac{C_p}{C_f}\right) \times 100\% \quad (3)$$

$$B = A(\Delta P - \Delta\pi)\left(\frac{1 - R}{R}\right) \quad (4)$$

where (C_p, g.L^{-1}) and (C_f, g.L^{-1}) are the solute concentrations of the permeate and feed solutions, respectively, and ($\Delta\pi$, bar) is the osmotic pressure difference across the membrane.

2.5.3 Stability test

The stability of the silica layer was assessed using the FO setup by subjecting the membrane to a cross-flow velocity of 12 cm.s^{-1} over 72 h at 20 °C using DI water. The membranes were then tested for FO performance, and the membrane surfaces were examined for hydrophilicity by measuring the water contact angles. The stability of silica layer when exposed to acid (HCl, pH=3), base (NaOH, pH=10) and salt (0.5 M NaCl) solutions was determined by shaking the membranes for 72 h at 70 rpm in the various solutions and measuring their water contact angles.

2.6 Membrane fouling test

The membrane fouling tests were conducted in four stages in the AL-FS mode using the FO setup. Firstly, baseline tests for the membranes were run with DI water FS and NaCl DS (0.5 M to 2 M) to adjust the initial baseline water flux ($J_{w,0}$) to ~20 L.m^{-2}.h^{-1} and determine the flux decline resulting from the DS dilution and J_s to the FS. Secondly, the accelerated fouling test was initiated at similar conditions as the baseline experiment by introducing 1 g.L^{-1} of foulant (BSA, HA and SA) into the FS containing 1 mM $CaCl_2$. BSA, HA and SA were picked as the model organic foulants to represent proteins, effluent organic matter (EfOM), and polysaccharides. The flux decline occurring, in this instance, resulted from the collective

influence of J_s, DS dilution and membrane fouling. Both the fouling and baseline tests were conducted at a flow rate of 250 mL.min^{-1} for ~17 h to obtain a cumulative permeate volume of 75 mL. The degree of fouling was quantified from the flux decline during the fouling test ($FD_{75\ mL}$) using Eq. (5) as reported earlier [39]:

$$FD_{75\ mL} = \frac{\left|\left(J_w/J_{w,0}\right)_{baseline} - \left(J_w/J_{w,0}\right)_{fouling}\right|}{\left(J_w/J_{w,0}\right)_{baseline}} \times 100\% \quad (5)$$

where the FD_{75mL} was measured from the normalized baseline and fouling fluxes $(J_w/J_{w,0})_{baseline}$ and $(J_w/J_{w,0})_{fouling}$, respectively. A lower bound of 0 for FD_{75mL} would indicate no occurrence of fouling; whereas, an upper bound of 100% would mean a complete loss in water permeability due to fouling.

Next, the fouled membranes were exposed to physical cleaning through the circulation of DI water in both DS and FS channels for 1 h at a higher flow rate of 500 mL.min^{-1}. An increased cross-flow velocity was used to generate additional hydraulic shear force during physical cleaning at the foulant layer to loosen and remove foulants on the membrane surface [40]. Lastly, the physically cleaned membranes were exposed to the baseline test conditions to evaluate the *FRR* using Eq. (6):

$$FRR = \frac{J_{w,0c}}{J_{w,0}} \quad (6)$$

where $J_{w,0}$ and $J_{w,0c}$ are the initial water fluxes of membranes before fouling and after cleaning, respectively.

3 Results and discussion

3.1 Membrane surface properties

The ultrathin silica layer was formed *in situ* on the PA TFC membrane surface, as illustrated in Figure 1. Firstly, the negatively charged TFC membrane was treated with hydrolyzed

positively charged APTES, which was adsorbed on the membrane surface through attractive electrostatic forces and hydrogen bonding. The positively charged aminosilane layer formed on the PA surface of the TFC membrane (APTES-TFC) through APTES self- condensation process, silanization reaction between APTES and the PA surface, and amide bond formation between the APTES amine and unreacted PA carboxylic acid groups [41]. Secondly, the aminosilane layer of the APTES-TFC membrane was exposed to a solution containing EtOH, ammonia and the negatively charged TEOS. Due to the electrostatic force of attraction, the TEOS monomers attached to the positively charged surface of the APTES-TFC membrane. Finally, the *in situ* silicification process occurred via the hydrolysis-condensation process of the adsorbed TEOS monomers on the APTES-TFC membrane surface; thus, forming an ultrathin silica layer via the nucleation and growth of nano-silica particles [42, 43].

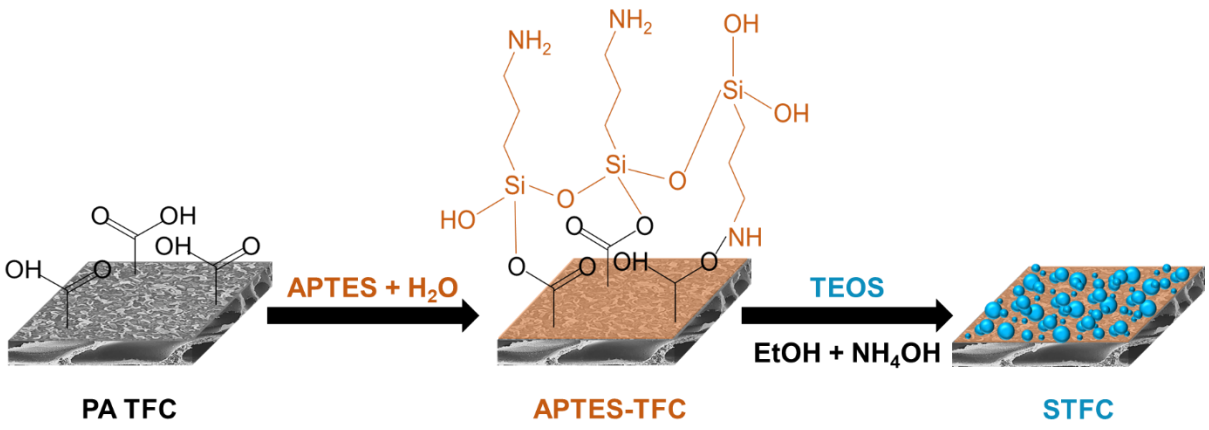

Figure 1: Schematic illustration of the procedure used to modify the PA TFC membrane surface via *in situ* silicification process. The blue spheres on the STFC membrane represent silica nanoparticles. APTES, H_2O, TEOS, EtOH and NH_4OH represent (3-aminopropyl)-triethoxysilane, water, tetraethoxysilane, ethanol and ammonium hydroxide, respectively.

The surface chemistries of the pristine TFC, APTES-TFC and resultant STFC membranes were examined using FTIR. As shown in Figure 2a, the FTIR spectra of all the membranes revealed the characteristic peaks of PSf at 1502 cm^{-1} (C=C aromatic ring in-plane scissoring vibration), 1385 cm^{-1} (symmetric C–H deformation of $C(CH_3)_2$), 1236 cm^{-1} (asymmetric C–O–C

stretching vibration of the aryl–O–aryl group), 1294 cm^{-1} and 1147 cm^{-1} (asymmetric and symmetric stretching vibrations of the O=S=O bonds of PSf) [44, 45]. The membranes also exhibited the typical peaks of PA at 1663 cm^{-1} (amide I band), 1609 cm^{-1} (aromatic amide band) and 1541 cm^{-1} (amide II band, N–H in-plane bending vibration and C–N stretching of PA's amide group) [38]. Since the STFC-1h, STFC-3h and STFC-5h membranes do not clearly show the silica-associated peaks due to the small amount of silica on the membrane surface, the FTIR spectrum of the STFC-8h membrane was also included to identify the peaks related to silica. The relative intensity of the peaks at 1070 cm^{-1} was higher for the APTES-TFC and STFC membranes compared to the TFC membrane due to the Si–O–Si stretching vibration resulting from the hydrolysis and condensation of APTES on the membrane surface during the self-polymerization process [35]. The STFC membranes also revealed the characteristic Si–OH stretching vibration peak of silica at 950 cm^{-1} [46]. The relative intensity of this particular peak augmented from STFC-1h to STFC-8h, indicating that higher silica content was obtained over longer silicification time. Meanwhile, we also observed a decrease in relative intensities of the characteristic PSf and PA bands with increasing silicification time, which demonstrated the successful silica deposition on the membrane surface. The broad band around 3330 cm^{-1} occurs from the overlapping peaks that are ascribed to the N–H and carboxyl group stretching vibration of the PA, and O–H stretching vibration of incomplete silanol group (Si–OH) condensation [47].

XPS measurements were also used to study the chemical composition alterations resulting from the surface modification of the TFC membrane during *in situ* silicification process. Both the qualitative and quantitative chemical analyses were performed with XPS for the pristine and modified TFC membrane surfaces. The wide and narrow-scan XPS spectra representing the carbon (C 1s), silicon (Si 2p), and oxygen (O 1s) elements for the pristine TFC, APTES-TFC and STFC membranes prepared at various silicification times are presented in Figure S1 and

Figure 2b-d, respectively, while their surface elemental compositions are summarized in Table 1. The large asymmetrical peak on the C 1s spectrum was deconvoluted into four peaks; the peaks at 284.5 eV (the non-oxygenated carbon with sp^2 and sp^3 hybridization, C–C) and 286.6 eV (C–O) are associated to the PSf substrate [48], while the peaks at 284 (C–O–Si, C–N) and 285.4 eV (C–Si) occur due to APTES treatment on the membrane surface [49]. The intensity of the C 1s peaks decreased at higher silicification duration because of the formation of thicker silica layers (Figure 2b). The Si 2p XPS spectra of the APTES-TFC and STFC membranes demonstrated a peak at 103 eV; thus, indicating the formation of Si–O bonds after the APTES treatment and silicification process (Figure 2c) [50]. The deconvoluted XPS spectrum of the O 1s showed the presence of three additional peaks: the C–O (533.1 eV) and S=O (531.8 eV) bands of the PSf substrate, and the Si-O peak (533 eV) from the silica coating (Figure 2d). The intensities of both the Si 2p and O 1s peaks were observed to increase with increasing silicification duration due to the development of a denser silica layer on the APTES-TFC membrane surface (Figure 2c and d). Consequently, the elemental compositions of Si and O increased from 16.7% to 29%, and 29.3% to 43.3%, respectively; while that of C decreased from 54.1% to 27.7% on increasing the silicification duration from 1 h to 5 h (Table 1). Overall, both FTIR and XPS analyses confirm the effective growth of silica on the PA layer surface.

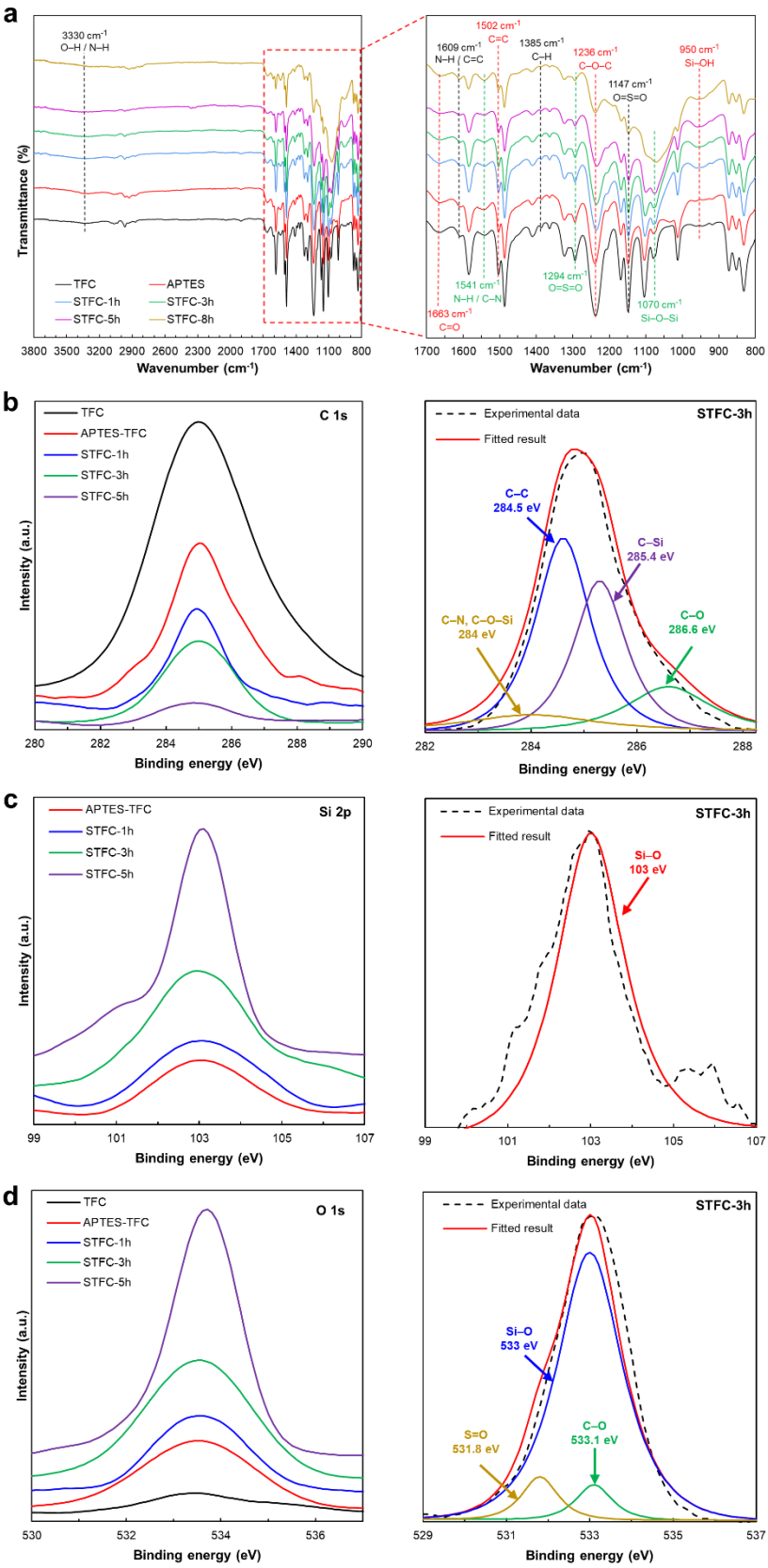

Figure 2: (a) FTIR spectra, and narrow-scan XPS spectra of (b) C, (c) Si, and (d) O elements of pristine and modified TFC membranes prepared at various silicification durations.

Table 1: Surface elemental compositions of the pristine and modified TFC membranes.

Membrane	C (%)	O (%)	Si (%)
TFC	85.8	14.2	0.0
APTES-TFC	70.7	20.8	8.6
STFC-1h	54.1	29.3	16.7
STFC-3h	40.9	38.2	21.0
STFC-5h	27.7	43.3	29.0

The surface and cross-section morphologies of the pristine and ultrathin silica-coated PA TFC membranes were systematically investigated via SEM (Figure 3) and AFM (Figure 5). The pristine TFC membrane demonstrated the characteristic ridge-and-valley structure of the PA layer (Figure 3a); thus, confirming the occurrence of IP process on the PSf substrate. The APTES-TFC membrane demonstrated similar morphology (Figure 3b) and roughness (Figure 5b) as that of the TFC membrane (Figure 3a and Figure 5a), which confirms that the APTES treatment had no significant influence on the morphology of the PA layer (Figure 3b and Figure 5b). However, the SEM images of the STFC-1h, STFC-3h and STFC-5h surfaces (Figure 3c-d) revealed more distinct morphologies with uniform deposition of silica nanoparticles, which implies that the *in situ* silicification process occurred successfully on the PA layer surface.

During the first hour of the silicification process, the hydrolysis-condensation reactions of the APTES and TEOS formed silica nuclei on the surface of STFC-1h as can be observed from Figure 3c. By prolonging the silicification time to 3 h, the silica nuclei grew bigger to form a more continuous silica layer on the STFC-3h surface (Figure 3d, left). However, the deposited silica nanoparticles were not visible on the SEM cross-section images (Figure 3d, right), which suggests the growth of an ultrathin silica layer that only influences the membrane surface chemistry without significantly changing the membrane morphology.

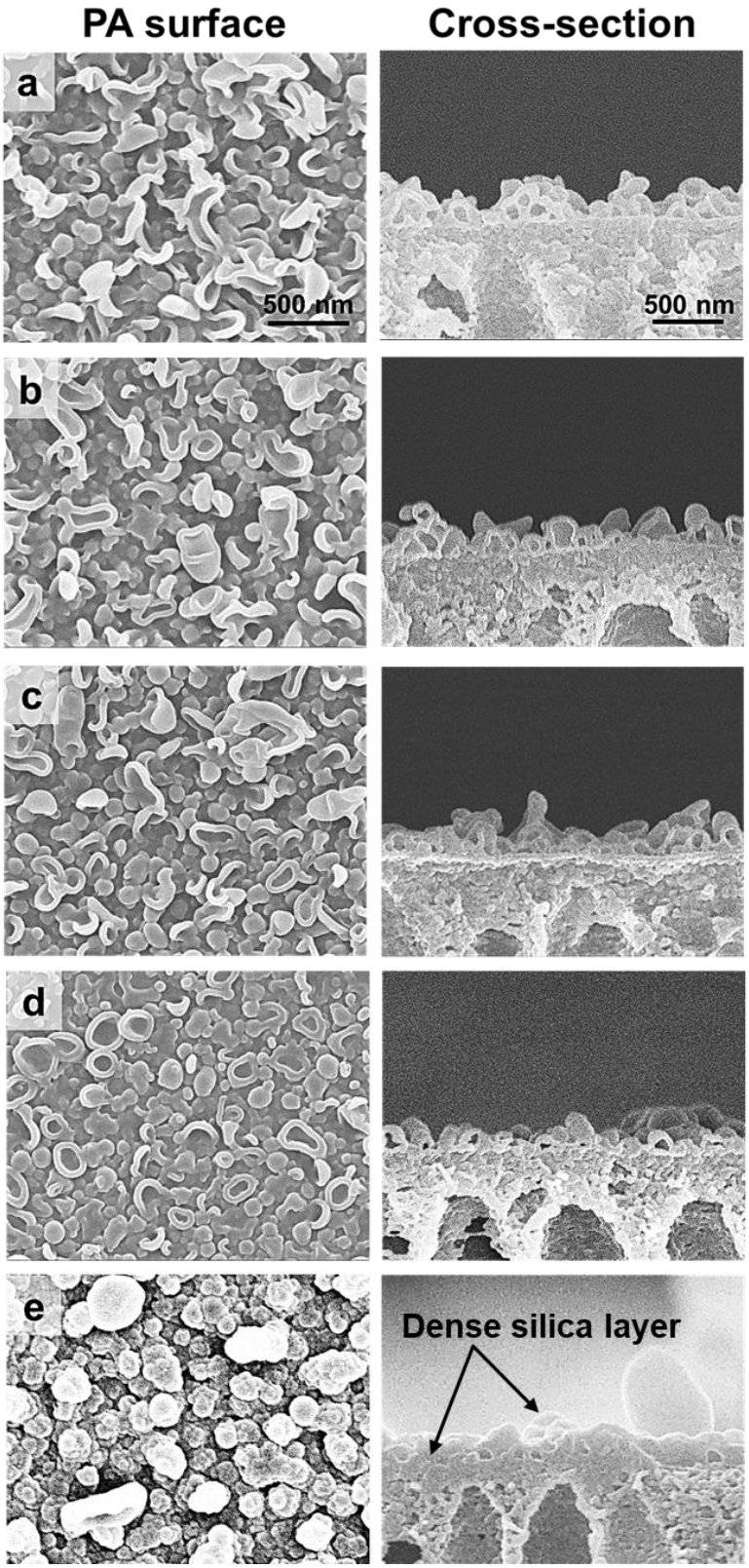

Figure 3: SEM images showing the top surface and cross-section morphologies of (a) pristine TFC, (b) APTES-TFC, (c) STFC-1h, (d) STFC-3h, and (e) STFC-5h membranes.

However, on further increasing the silicification time to 5 h, we observed a denser and thicker interconnected layer of silica clusters that mostly covered and penetrated the PA surface as demonstrated by the surface and cross-section SEM images of the STFC-5h membrane (Figure 3e). The larger-sized silica nanoparticles emerged due to collision and coagulation of the silica nuclei that were continuously in random motion to form a ~370 nm thick silica layer (Figure 3e) [35]. These results confirm that the size of silica particles and the thickness of the silica layer on the surface of the membrane could be easily adjusted through varying the silicification time.

The EDS mapping and spectra of the pristine TFC and silica-modified STFC membranes are presented in Figure 4. It can be observed from the EDS elemental mapping results of Si and O that silica (SiO_2) is uniformly distributed on the surface of the STFC membrane. Since silica is not grown on the surface of the pristine TFC membrane, the Si peak is missing from its EDS spectrum (Figure 4a). The orange dots on the EDS elemental mapping of the TFC membrane do not indicate the presence of Si, but result from the background noise.

In contrast, the EDS spectrum of the STFC membrane showed more intense Si and O peaks than that of the TFC membrane due to silica deposition on its surface (Figure 4b). The EDS mapping results of the STFC membrane's cross-section SEM image showed a thin layer of Si on its surface (Figure 4c), which further confirms that a thin silica layer was mainly deposited on the PA layer surface without obvious intrusion into the porous PSf substrate.

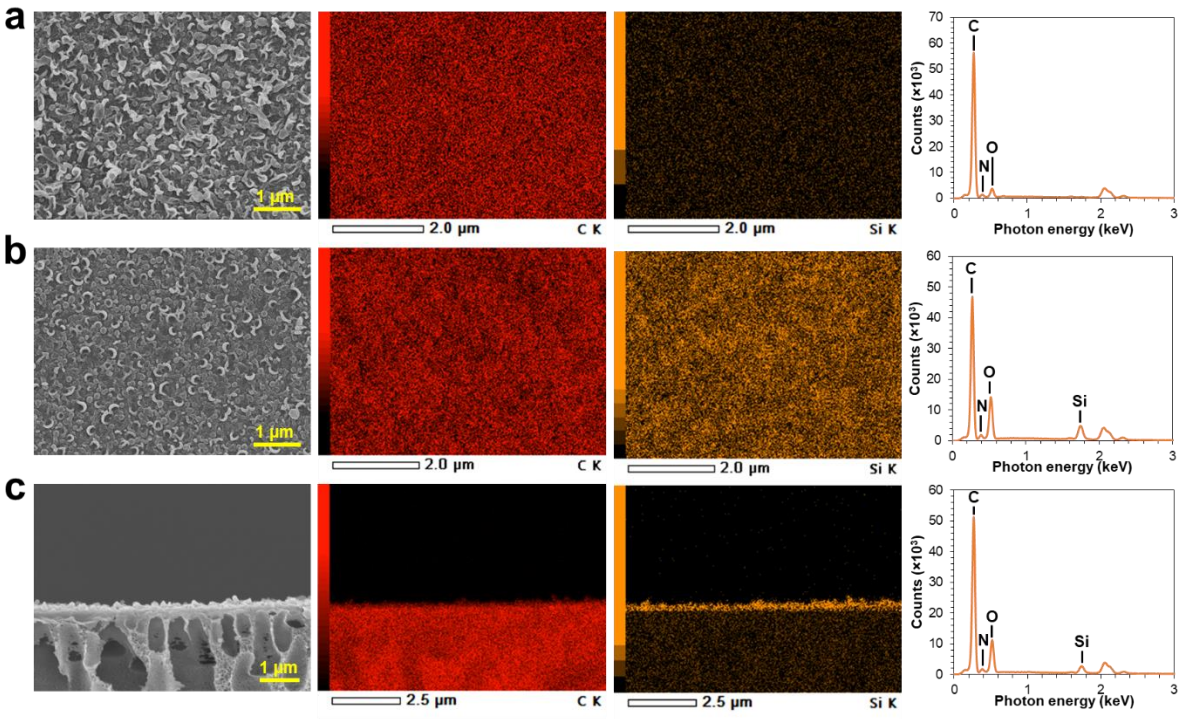

Figure 4: SEM, EDS mapping and EDS spectra of (a) pristine TFC membrane top surface, (b) silica-coated STFC membrane top surface and (c) silica-coated STFC membrane cross-section. Red and orange dots on EDS mapping indicate signals of carbon (C) and silica (Si), respectively.

As evident from AFM topography results, the surface of the STFC membranes became rougher as the silicification process duration was increased from 1 h to 5 h (Figure 5). The average surface roughness (R_a) of the silica-modified PA TFC membranes increased from 54.1 nm for STFC-1h to 58.4 nm for STFC-3h and 81.1 nm for STFC-5h membranes due to the formation of larger silica clusters on the PA surface (Figure 5c-e). The pristine TFC and APTES-TFC membranes demonstrated comparatively smoother surfaces with near-identical R_a values of 39.8 and 40.6 nm, respectively (Figure 5a and b). This observation further confirms that the APTES treatment did not considerably modify the morphology of the TFC membrane but primarily modified its surface chemistry, which will be verified later from the contact angle and surface zeta potential measurements.

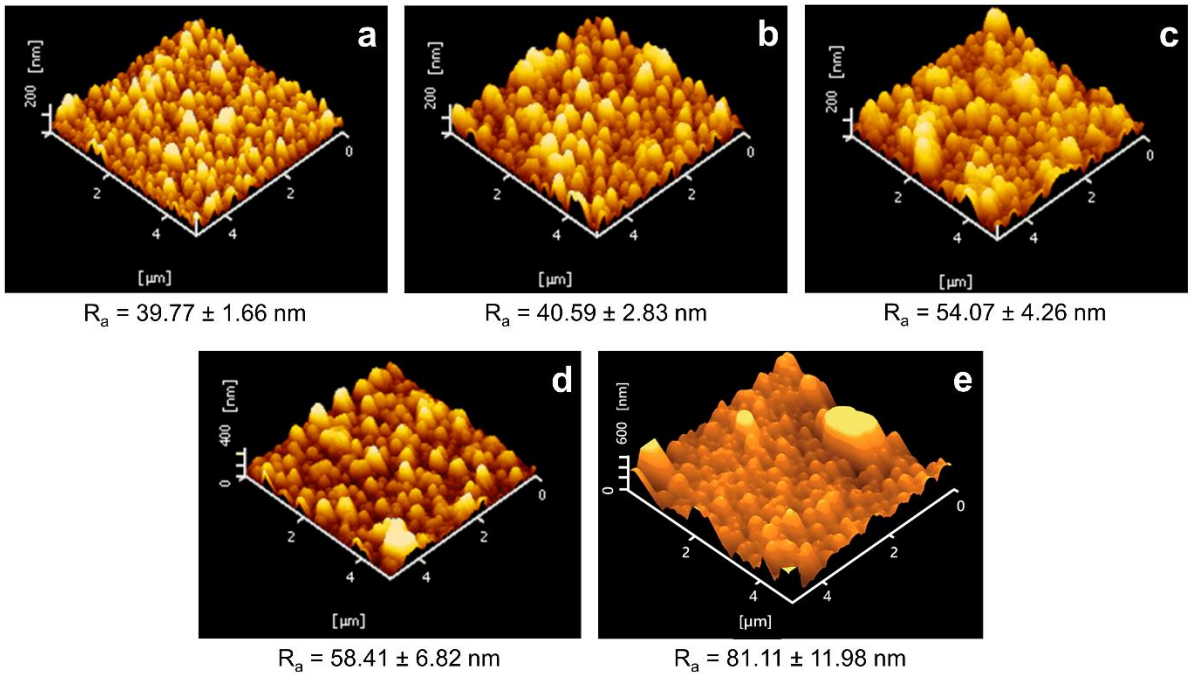

Figure 5: AFM topography images representing membrane surface roughness of (a) pristine TFC, (b) APTES-TFC, (c) STFC-1h, (d) STFC-3h, and (e) STFC-5h membranes. Error bars for membrane surface roughness represent one standard error obtained from at least 3 membrane samples for each condition.

The membrane surface wettability of the pristine TFC, APTES-TFC and silica-coated STFC membranes was determined from the initial water contact angles measured on their surfaces. As can be observed from Figure 6a pristine TFC membrane possessed the least hydrophilic surface before water rinsing with a contact angle of 71°. The TFC membrane's surface hydrophilicity improved slightly after 16 h of APTES treatment (APTES-TFC) and exhibited a water contact angle of 68°. However, the silica-coated STFC membranes displayed a significant improvement in wettability with lower water contact angles. Specifically, the water contact angles declined from 41° for STFC-1h to 15° for STFC-5h due to deposition of more silica on the membrane surface. The observed trend in membrane hydrophilicity suggests that the silica coating can improve the membrane hydrophilicity as it comprises of a considerable amount of hydrophilic silanol and related hydroxyl groups.

To determine the stability of the silica layer on the STFC membranes, the membranes were subjected to rinsing at a higher cross-flow velocity of 12 $cm.s^{-1}$ for 72 h at room temperature using DI water. As expected, the initial water contact angle of the TFC membrane did not change after rinsing (Figure 6a). The APTES-TFC membrane also revealed similar water contact angles before and after rinsing, which confirms the stability of the aminosilane layer under the applied high shear operating conditions. The hydrophilicity of the STFC-1h membrane, on the other hand, significantly declined with the water contact angle increasing from 41° to 58° after high shear rinsing possibly because of the weak adhesion of silica particles to the membrane surface. The STFC-3h and STFC-5h membranes also exhibited reduced hydrophilicity after DI water rinsing, but their water contact angles increased only by 3.3° and 2.3°, respectively, which is insignificant compared to that of the STFC-1h membrane. Hence, it can be concluded that the stability of the silica layer increased at higher silicification time.

The surface charge of the TFC, APTES-TFC and silica-modified STFC membranes are shown in terms of the zeta potential measurements over a pH range of 3 to 10, as presented in Figure 6b. The pristine TFC membrane was observed to be positively charged at pH <3.5 due to the protonation of the PA layer's pendant amino groups. At pH >3.5, the pristine TFC membrane exhibited a negatively charged surface owing to the deprotonation of the PA layer's carboxyl and amino groups [51]. The negatively charged surface of the TFC membrane facilitated adsorption of positively charged APTES on its surface via attractive electrostatic forces, in addition to hydrogen bonding. As revealed by Figure 6b, the aminosilane layer that formed on the PA layer from the hydrolysis and self-condensation of APTES rendered the TFC membrane surface positively charged (APTES-TFC), which further assisted in the adsorption of negatively charged TEOS via electrostatic interaction to form an ultrathin silica coating through *in situ* silicification process [41].

The formation of silica layer on PA surface subsequently reversed the membrane surface charge from positive (APTES-TFC) to negative (STFC-1h, STFC-3h and STFC-5h) [35, 52]. In summary, the TFC membrane revealed the most negatively charged surface because of the presence of abundant carboxyl groups. In contrast, the negative surface charge of the STFC membranes was lower compared to the pristine membrane owing to the silica layer's shielding effect that reduced the exposure of PA layer's carboxyl groups [53]. Moreover, the zeta potentials for the STFC membranes progressively became more negative as the silicification duration was increased from 1 h (STFC-1h) to 5 h (STFC-5h) due to the formation of more silica particles that contained abundant negatively charged hydroxyl groups [54].

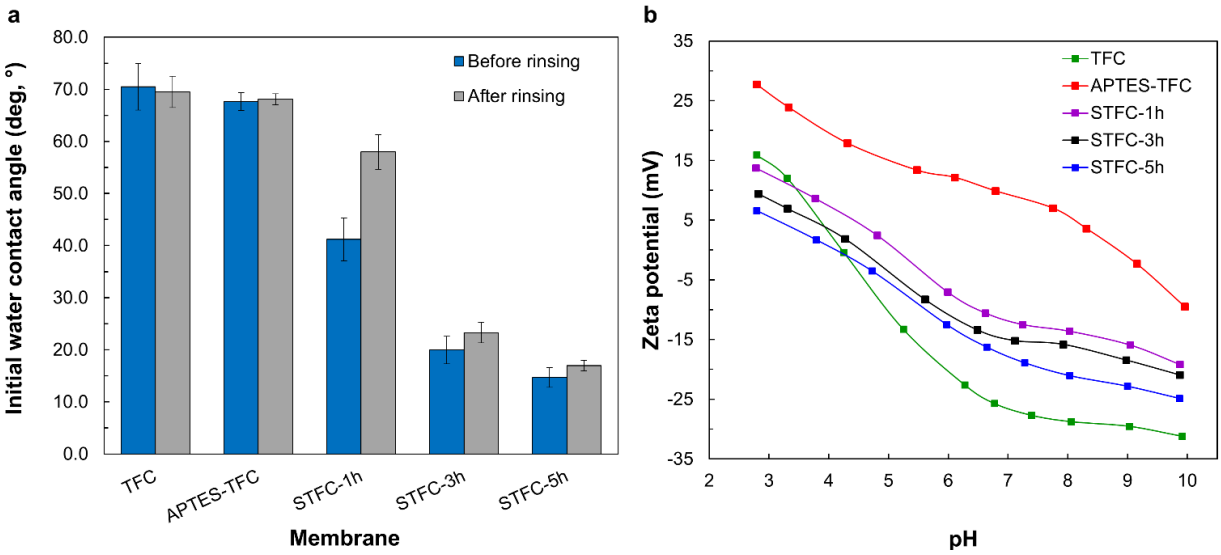

Figure 6: (a) Initial water contact angle measurements of the pristine and modified TFC membranes before and after rinsing with DI water for 72 h at a co-current cross-flow velocity of 12 cm.s^{-1}. Error bars for initial water contact angle measurements represent one standard error obtained from at least 7 measurements for each membrane sample. (b) Surface zeta potential measurements of the pristine and modified TFC membranes.

3.2 FO membrane performance

The FO performances of the pristine TFC, APTES-TFC and STFC membranes were determined in AL-FS orientation using 1 M NaCl as DS and DI water as FS. The reverse solute flux (J_s), water flux (J_w) and specific reverse solute flux (*SRSF*) across the prepared membranes

are presented in Figure 7. Due to the improved surface hydrophilicity of the APTES-TFC membrane, it showed a higher J_w (20 L.m^{-2}.h^{-1}) compared to that of the pristine TFC membrane (17 L.m^{-2}.h^{-1}). The J_s of the APTES-TFC membrane, however, remained similar as that of the TFC membrane (~6.4 g.m^{-2}.h^{-1}), which confirmed that 16 h of APTES treatment altered the membrane surface properties without impairing the PA layer. The STFC-1h showed a similar J_w as that of the APTES-TFC membrane possibly due to formation of an unstable silica coating that partially washed off during the test as observed from the increase in its water contact angle measurements after rinsing (Figure 6a). Owing to the improved stability of the silica layer on the STFC-3h membrane, as evident from its water contact angle results (Figure 6a), it demonstrated the highest J_w of 26 L.m^{-2}.h^{-1} with a small increase in the J_s (6.9 g.m^{-2}.h^{-1}) as a result of the permeability-selectivity trade-off relationship. Both the J_w and J_s of the STFC-5h membrane (14 L.m^{-2}.h^{-1} and 2.5 g.m^{-2}.h^{-1}, respectively) were the lowest compared to other membranes due to the increased hydraulic resistance from the dense silica layer formation that nearly covered the entire PA layer surface, as observed earlier from the SEM images (Figure 3e). Although STFC-5h membrane revealed the most hydrophilic surface, its thicker silica layer negatively impacted the J_w as a consequence of the additional hydraulic resistance. The dense silica layer, however, improved the selectivity of the membrane by allowing fewer DS ions to pass through from the DS to FS; consequently, diminishing the J_s of the STFC-5h membrane.

The *SRSF* is an essential parameter in the FO process, which specifies the selectivity of the FO membranes. A lower *SRSF* value is preferable as it denotes a more selective membrane. As shown in Figure 7, APTES treatment of the TFC membrane reduced its *SRSF* value by 16% in comparison to the TFC membrane. Likewise, the modified TFC membranes with silica layer attained lower *SRSF* values in comparison to the TFC membrane owing to their relatively higher J_w with similar J_s resulting from their increased hydrophilicity. Specifically, the highest

SRSF value of 0.38 $g.L^{-1}$ was observed for the TFC membrane because of the looser pore structure of its PA layer, which facilitated relatively more DS ions to move to the FS from the DS. The STFC-1h (0.26 $g.L^{-1}$) and STFC-3h (0.27 $g.L^{-1}$) showed comparable SRSF values, but that of STFC-5h (0.17 $g.L^{-1}$) was significantly smaller due to the augmented hydraulic resistance occurring from its dense silica layer. The STFC-3h was selected as the most favourable membrane as it revealed the highest J_w in comparison to other silica-modified TFC membranes without deteriorating its selectivity.

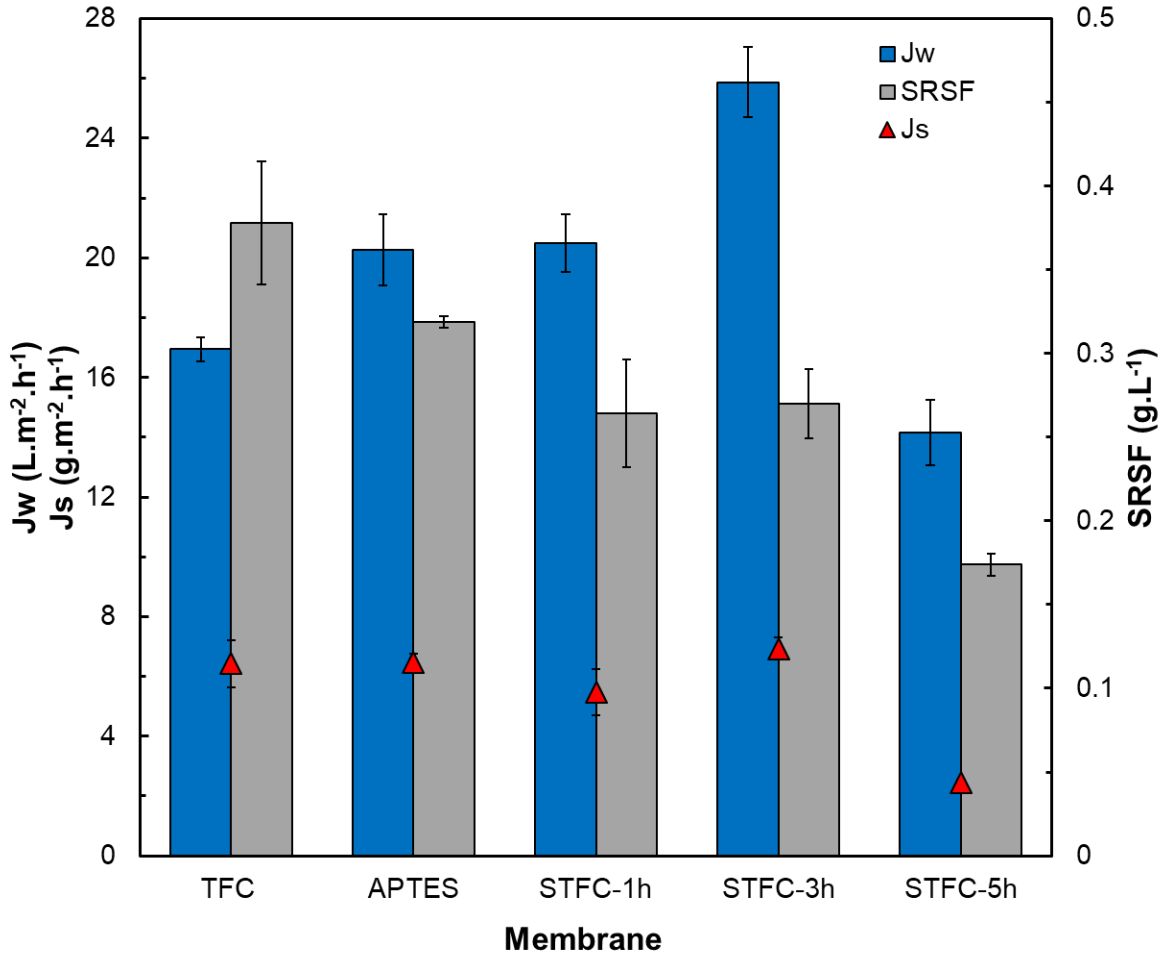

Figure 7: FO performance of the pristine and modified TFC membranes with 1 M NaCl as DS and DI water as FS in AL-FS arrangement at a co-current cross-flow velocity of 12 $cm.s^{-1}$. Error bars represent one standard error obtained from the performance results of at least 3 membrane samples at each condition.

The intrinsic transport properties of the pristine and modified TFC membranes were determined from the pure water permeability coefficient (*A*), solute permeability coefficient (*B*), and intrinsic membrane selectivity ratio (*B/A*) as listed in Table 2. The APTES-TFC membrane with the aminosilane layer and the silica-coated STFC-1h and STFC-3h membranes demonstrated higher *A* values (2.14, 2.18 and 2.46 $L.m^{-2}.h^{-1}.bar^{-1}$, respectively) in comparison with the pristine TFC membrane (2.08 $L.m^{-2}.h^{-1}.bar^{-1}$) due to their improved surface hydrophilicity. The *B* values of the modified membranes showed a similar trend as that of the membrane J_s during the FO performance due to the same reasons as discussed above. However, the STFC-5h membrane displayed the lowest *A* (1.78 $L.m^{-2}.h^{-1}.bar^{-1}$) and *B* (0.43 $L.m^{-2}.h^{-1}$) values due to the development of a dense silica layer on its surface that reduced its water permeability and increased the draw solute selectivity by increasing the hydraulic resistance across it. The least selective TFC membrane showed the largest *B/A* ratio of 0.36 bar; whereas, the STFC-5h was found to be the most selective with the smallest *B/A* ratio of 0.24 bar. Both STFC-1h and STFC-3h membranes exhibited similar selectivity with *B/A* ratios of 0.29 bar and 0.31 bar, respectively. The intrinsic transport parameters are in good agreement with the FO performance of the membranes presented in Figure 7 and validated that the membrane performance could be adjusted by tuning the silicification time.

Table 2: Intrinsic transport parameters of pristine and modified TFC FO membranes. Error bars represent one standard error obtained from at least 3 membrane samples for each condition.

Membrane	*A* ($L.m^{-2}.h^{-1}.bar^{-1}$)	*B* ($L.m^{-2}.h^{-1}$)	*B/A* (bar)
TFC	2.08 ± 0.26	0.75 ± 0.06	0.36 ± 0.013
APTES-TFC	2.14 ± 0.19	0.73 ± 0.10	0.34 ± 0.014
STFC-1h	2.18 ± 0.09	0.63 ± 0.04	0.29 ± 0.005
STFC-3h	2.46 ± 0.18	0.76 ± 0.07	0.31 ± 0.005
STFC-5h	1.78 ± 0.17	0.43 ± 0.02	0.24 ± 0.010

3.3 Membrane stability

The durability and stability of the membrane coating are crucial factors to evaluate their scale-up potential for practical applications. Therefore, the optimal STFC-3h membrane was subjected to a high co-current cross-flow velocity shear of 12 cm.s^{-1} operated for 72 h using DI water to assess the mechanical stability of the silica-coating on the TFC membrane surface. As presented in Figure 8a, the STFC-3h membrane revealed identical FO performance both before and after intense rinsing with DI water; thus, demonstrating that the silica coating remained mechanically stable over the long-term cross-flow rinsing process. The FO test results are in good conformity with the contact angle measurements, as discussed earlier (Figure 6a).

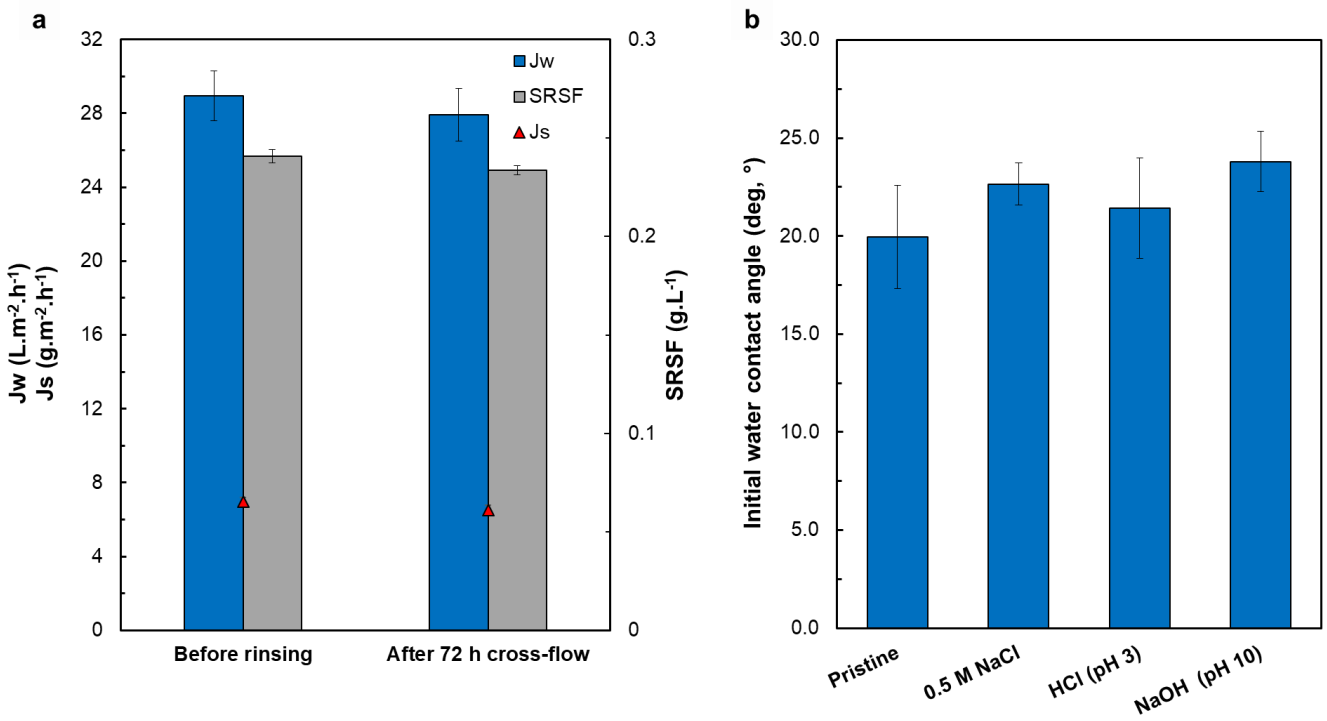

Figure 8: a) FO performance of STFC-3h membrane before and after rinsing with DI water for 72 h at a co-current cross-flow velocity of 12 cm.s^{-1}. The membranes were tested in AL-FS arrangement with 1 M NaCl as DS and DI water as FS at a co-current cross-flow velocity of 12 cm.s^{-1}. b) Initial water contact angle measurements of the STFC-3h membrane before and after its exposure to the salt solution (0.5 M NaCl), acid (HCl, pH 3) and base (NaOH, pH 10) for 72 h at 70 rpm. Error bars for FO performance (initial water contact angle measurements) represent one standard error obtained from at least 2 membrane samples (5 random positions) for each condition.

The STFC-3h membrane was also treated with salt, acid and base to investigate its chemical stability under various conditions, as shown in Figure 8b. It was found that STFC-3h membrane exhibited only 2.7° increase in water contact angle after exposing to a 0.5 M NaCl solution by constant shaking for 72 h, suggesting excellent chemical stability. Similarly, the treatment of STFC-3h membrane with HCl and NaOH showed only a slight rise in water contact angle by 1.4° and 3.8°, respectively, which is within the measurement error range. These results proved that the silica layer on the STFC-3h membrane surface remained stable under various chemical exposures, which could be attributed to the exceptional adhesion force between the silica and aminosilane layers via stable covalent Si–O–Si bonds. These results also suggest that the STFC-3h membrane can be suitably applied under harsh environments.

3.4 Antifouling properties

The antifouling properties of the pristine TFC and STFC-3h membranes were examined using accelerated fouling experiments using different organic foulants (BSA, HA and SA), where the foulant dosage in the FS was maintained at 1 $g.L^{-1}$. Both BSA and SA were selected to represent the higher molecular weight compounds present in wastewaters and surface waters; while, HA was chosen to demonstrate the effect of hydrophobic characteristics of the organic matter on the membrane fouling propensity. The normalized flux decline corresponding to 75 mL of permeate volume (FD_{75mL}) against different organic foulants is presented in Figure 9. As can be observed, the STFC-3h membrane showed a suggestively lower FD_{75mL} compared to the TFC membrane with all the foulants, indicating that the surface modification of PA layer with silica layer can improve the antifouling properties of the membrane as a result of its improved hydrophilicity. The TFC membrane's poor antifouling property could be attributed to the development of a dense foulant layer on its surface owing to the strong interaction forces between its more hydrophobic surface and the organic foulants.

The flux decline in both TFC and STFC-3h membranes with BSA and HA was considerably lower than that with SA. For instance, STFC-3h (TFC) revealed a FD_{75mL} of 4.2% and 9.1% (18.7% and 23.2%) with BSA and HA, respectively, which is relatively lower than a FD_{75mL} of 12.14% (37.2%) obtained with SA. These results indicate that both BSA and HA do not adhere to the membrane surfaces easily compared to SA, which resulted in a lower flux decline. The more serious SA fouling could be ascribed to the Ca^{2+} bridging effect between the ions and the abundant carboxylic functional groups forming a highly cross-linked foulant layer on the membrane surface [38, 55]. Since the BSA molecules contain only a low amount of carboxylic groups, the presence of Ca^{2+} in the FS has minor influence on the BSA fouling tendency [56].

In comparison to the TFC membrane, the STFC-3h membrane exhibited a suggestively better antifouling property to all the foulants owing to the existence of fewer carboxyl groups on its surface. The *in situ* APTES treatment and silicification process on the PA layer partially occupied the carboxyl groups on the PA layer, which effectively diminished the inter-adhesion between foulants and the membrane surface; thus, leading to the lower membrane fouling potential. The hydrophilic silica coating on the STFC-3h membrane also mitigated fouling by forming a water barrier between the hydrophobic foulants and the membrane surface that weakened the interfacial interaction between them [22, 57]. Overall, the fouling test results confirm that the membrane surface properties can significantly impact the membrane fouling behaviour, and that weakening the foulant-membrane interfacial interaction could reduce foulant accumulation on the membrane surface; thereby, reducing the membrane flux decline.

After the completion of the fouling tests, the membranes were exposed to simple physical cleaning with DI water for 1 h at a higher cross-flow velocity of 0.5 $L.min^{-1}$ and tested under the initial baseline conditions to assess their *FRR*. As presented in Figure 9, the STFC-3h membrane achieved a greater *FRR* than that of the TFC membrane under all conditions due to its more hydrophilic surface, which weakened the foulant–membrane and foulant–foulant interactions.

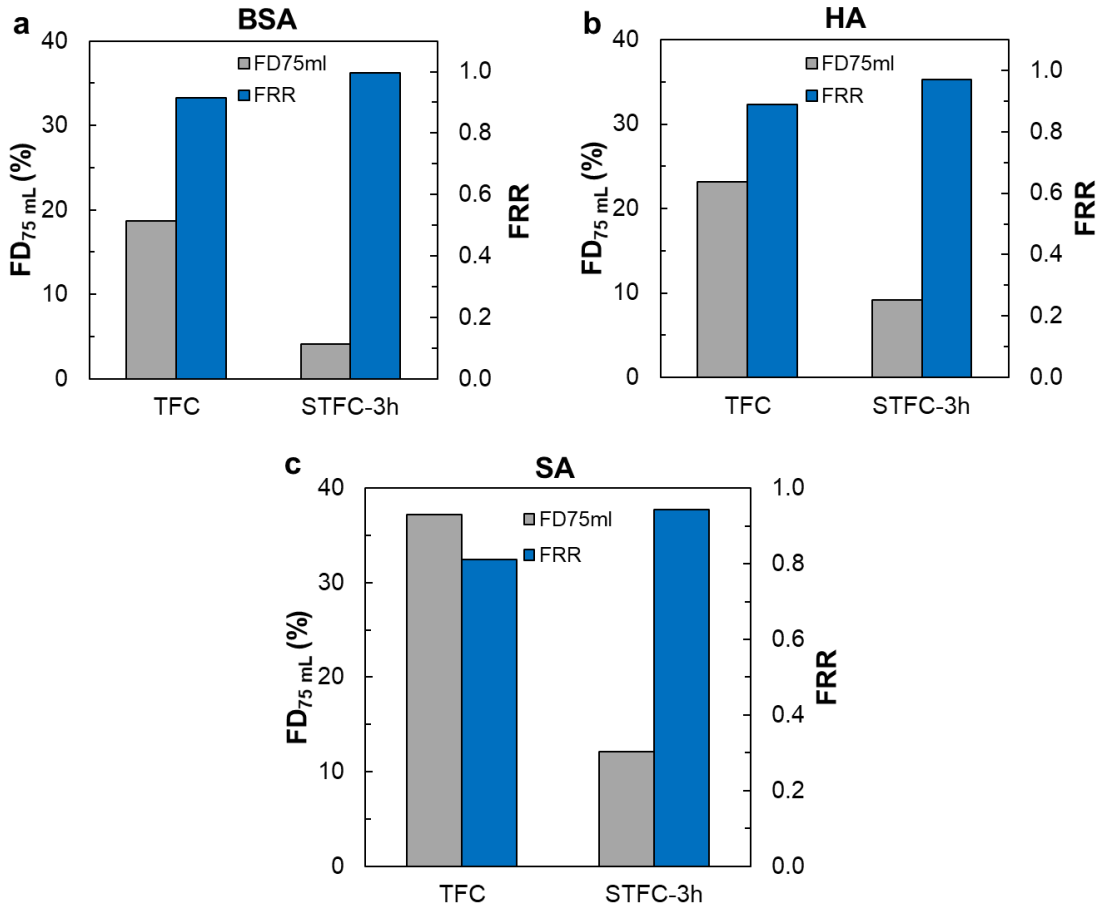

Figure 9: The normalized flux decline (FD_{75mL}) during the accelerated fouling test with 1 g.L^{-1} a) BSA, b) HA, and c) SA, and the *FRR* after physical cleaning of the pristine TFC and modified STFC-3h membranes. Operating conditions: Initial baseline water flux ($J_{w,0}$), ~20 L.m^{-2}.h^{-1}; membrane orientation, AL-FS; DS, 0.5-2 M NaCl; foulants, 1 mM calcium chloride and 1g.L^{-1} BSA/HA/SA; flow rate (baseline and fouling test), 0.25 L.min^{-1}; flow rate (physical cleaning), 0.5 L.min^{-1}.

Both the TFC and STFC-3h membranes revealed increased normalized flux after the physical cleaning, which indicates the fouling reversibility of the membranes up to a certain extent. The *FRR* of the TFC membrane was 91.4% and 88.7%; whereas, that of STFC-3h membrane was 99.6% and 96.9% after BSA and HA fouling, respectively. In the case of SA fouling, the TFC membrane attained a small *FRR* of 81.2%, suggesting substantial irreversible fouling because of strong adhesion of the SA layer on the membrane surface. However, the STFC-3h membrane exhibited a comparatively higher flux recovery of 94.4% after SA fouling due to its hydrophilic surface that contained less carboxylic functional groups and foulant adhesive sites, which

allowed a greater extent of foulant removal from its surface. Consequently, the improved antifouling property of the STFC-3h membrane diminished the foulant-membrane interaction by facilitating the development of a loosely adhered foulant layer that could be eradicated by simple hydraulic rinsing. It could be concluded from the fouling tests that the BSA and HA fouling is more reversible than the SA fouling, and that the membrane cleaning efficiency is governed by the severity of foulant-foulant and foulant-membrane interactions.

4 Conclusions

In this work, surface modification of PA TFC membranes was explored by varying the duration of *in situ* silicification process to form an ultrathin silica layer on the PA membrane surface. The density of silica coating on the PA layer surface and its surface wettability and surface charge increased with an increase in the silicification duration; however, 3 h was observed to be the optimum duration beyond which the water transport resistance across the membrane increased. The optimum membrane (STFC-3h) demonstrated the best silica coating stability and FO process performance with the highest water enhancement of 53% while retaining membrane selectivity in AL-FS orientation in comparison to the pristine TFC membrane. The improved FO performance could be ascribed to the enhanced surface hydrophilicity resulting from the hydrophilic silica coating. The inorganic silica coating on the STFC-3h membrane surface also showed good mechanical stability when subjected high cross-flow shear rinsing with DI water for 72 h and also when exposed to salty, acidic and basic solutions. Moreover, the hydrophilic STFC-3h membrane revealed improved antifouling property and *FRR* than that of the TFC membrane when exposed to BSA, HA and SA fouling by reducing the foulant-membrane and foulant-foulant interactions. Overall, the facile *in situ* silicification technique for membrane PA surface modification shown in this study opens up a promising pathway to augment the FO performance and antifouling properties of the PA TFC membranes.

Credit author statememt

Nawshad Akther: Data curation; Formal analysis; Investigation; Methodology, Validation; Visualization; Roles/Writing - original draft; Writing - review & editing.

Yuqing Lin: Data curation; Formal analysis; Investigation; Methodology.

Shengyao Wang: Data curation; Formal analysis; Investigation; Methodology.

Sherub Phuntsho: Supervision; Project administration; Resources; Data curation.

Qiang Fu: Review & editing, Discussion.

Noreddine Ghaffour: Writing - review & editing, Discussion.

Hideto Matsuyama: Writing - review & editing, Discussion.

Ho Kyong Shon: Supervision; Project administration; Resources; Funding acquisition; Validation; Visualization; Roles/Writing - original draft; Writing - review & editing.

Declaration of competing interest

The authors declare that they have no known competing financial interests or personal relationships that could have appeared to influence the work reported in this paper.

Acknowledgement

The research reported in this paper was supported by the ARC Industrial Transformation Research Hub (IH170100009) and the King Abdullah University of Science and Technology (KAUST), Saudi Arabia through the Competitive Research Grant Program – CRG2017 (CRG6), Grant # URF/1/3404-01.

Appendix A Supplementary Information

S1. Membrane fabrication

S1.1. Polysulfone membrane substrate

A homogenous polymer solution was prepared by dissolving 12 wt% polysulfone (PSf) in 1-methyl-2 pyrrolidone (NMP) at 60 °C and stirring at 500 rpm continuously for 12 h. The well-mixed PSf dope solution was then left for degassing overnight at room temperature. The degassed PSf dope solution was then cast on a glass plate with a 120 µm casting knife height and immediately immersed into a water coagulation bath at 20 °C for substrate formation. The phase inversion process was initiated by immediately immersing the PSf film-coated glass sheet in a coagulation bath holding water at room temperature. The PSf substrate was next rinsed thoroughly with and stored in deionized (DI) water at 4 °C for at least 24 h to eradicate the residual solvents.

S1.2. Polyamide active layer

The fabricated substrate was first wetted with DI water and fixed on a rectangular frame. Any remaining water on the substrate surface was then eliminated with an air knife. Interfacial polymerization (IP) was used to create a selective polyamide (PA) layer on the substrate. The substrate was first submerged for 2.5 min in *m*-phenylenediamine (MPD) aqueous solution (4 wt%). Filter paper and nitrogen knife were then employed to eradicate the surplus MPD from the substrate, which was then immersed for 1 min in 1,3,5-benzenetricarbonyl trichloride (TMC)/n-hexane organic solution (0.1 wt%). Next, the membrane was cured for 5 min at 60 °C to improve the PA cross-linking degree. Finally, the TFC FO membrane was washed carefully under running DI water for 3 min to eradicate any residual chemical. Lastly, the membranes were immersed in DI water and stored at 4 °C before testing their performance.

S2. FO membrane performance assessment

The membrane water flux (J_w, L.m^{-2}.h^{-1}) was determined using Eq. S1 from the weight of feed solution (FS), which was logged automatically at a constant time interval by digital weight balance, where ΔV_{FS} (L) is the change in the feed solution (FS) volume during the performance test, A_m, (m^2) is the effective membrane surface area and Δt (h) is the duration of the performance test.

$$J_w(L.m^{-2}.h^{-1}) = \frac{\Delta V_{FS}}{A_m \Delta t} \quad \text{(S1)}$$

The reverse solute flux (J_s, g.m^{-2}.h^{-1}) through the membrane was calculated using Eq. S2 by monitoring the FS salinity with a conductivity meter, where ΔC_{FS} (g.L^{-1}) is the change in the concentration of FS after an interval of Δt (h).

$$J_s(g.m^{-2}.h^{-1}) = \frac{\Delta C_{FS} V_{FS}}{A_m \Delta t} \quad \text{(S2)}$$

The specific reverse solute flux *SRSF* (g.L^{-1}), which indicates membrane selectivity, was obtained using Eq. S3.

$$SRSF(g.L^{-1}) = \frac{J_s}{J_w} \quad \text{(S3)}$$

S3. Membrane characterization

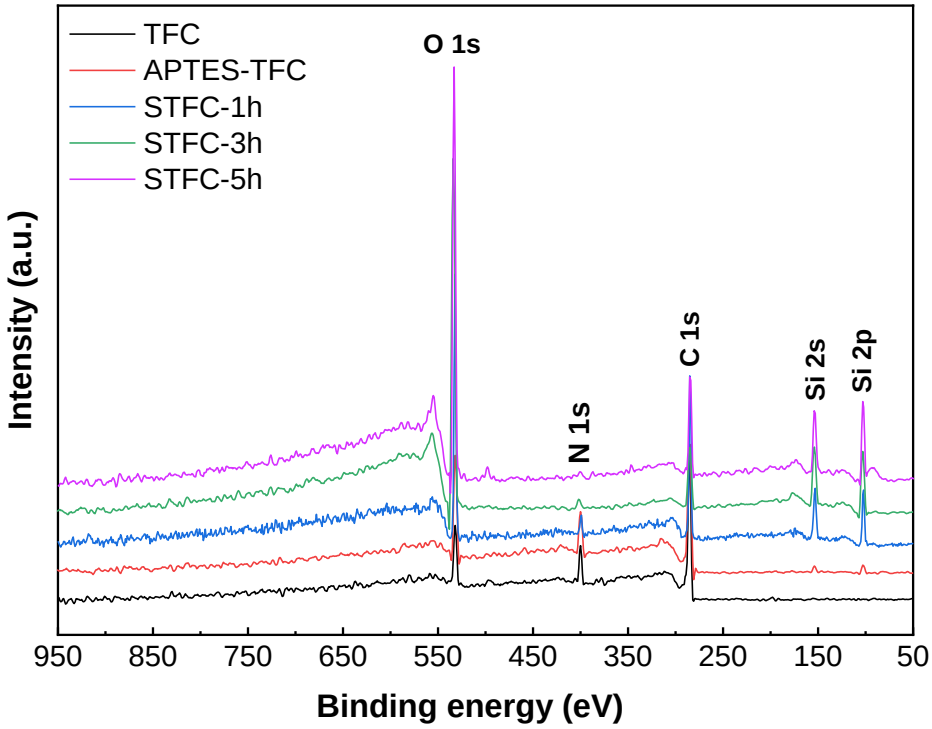

Figure S1: Wide-scan XPS spectra of pristine and silica-modified TFC membranes prepared at various silicification durations

Abbreviations

AFM:	Atomic force microscopy
ALD:	Atomic layer deposition
AL-FS:	Active layer oriented towards feed solution
APTES:	Aminopropyltriethoxysilane
ASP:	Alternate soaking process
BSA:	Bovine serum albumin
$CaCl_2$:	Calcium chloride
DI:	De-ionized water
DS:	Draw solution
EDS:	Energy-dispersive X-ray spectroscopy
EfOM:	Effluent organic matter
EtOH:	Ethanol
FESEM:	Field emission scanning electron microscopy
FO:	Forward osmosis
FS:	Feed solution
FRR:	Flux recovery ratio
FTIR-ATR:	Fourier-transform infrared spectroscopy with attenuated total reflectance
HA:	Humic acid
HCl:	Hydrochloric acid
IEP:	Isoelectric point
IP:	Interfacial polymerization
LbL:	layer-by-layer
MPD:	1,2-phenylenediamine
NaCl:	Sodium chloride
NaOH:	Sodium hydroxide
NIPS:	Non-solvent induced phase separation
NMP:	1-methyl-2-pyrrolidone
PA:	Polyamide
PSf:	Polysulfone
RO:	Reverse osmosis
SA:	Sodium alginate
SEM:	Scanning electron microscope
TEOS:	Tetraethoxysilane
TFC:	Thin-film composite
TFN:	Thin-film nanocomposite
TMC:	Trimesoyl chloride
XPS:	X-ray photoelectron spectroscopy

Nomenclature

$\Delta\pi$:	Osmotic pressure difference across the membrane
A:	Pure water permeability coefficient ($L.m^{-2}.h^{-1}.bar^{-1}$)
A_m:	Effective area of membrane (m^2)
B:	Solute permeability coefficient ($L.m^{-2}.h^{-1}$)
B/A:	Intrinsic membrane selectivity (bar)
C_p:	Solute concentration of the permeate solution ($g.L^{-1}$)
C_f::	Solute concentration of the feed solution ($g.L^{-1}$)
ΔC_{FS}:	Change in the feed solution concentration after an interval of Δt ($mg.L^{-1}$)
FD:	Flux decline during the fouling test (%)
J_s:	Reverse solute flux ($g.m^{-2}.h^{-1}$)
J_w:	Water flux ($L.m^{-2}.h^{-1}$)
M:	Molar concentration ($mol.L^{-1}$)
ΔP	Applied pressure difference (bar)
R:	Solute rejection (%)
R_a:	Mean value of membrane surface roughness (nm)
$SRSF\ (J_s/J_w)$:	Specific reverse solute flux ($g.L^{-1}$)
Δt:	Time interval (h)
V_{FS}:	Feed solution volume (L)
ΔV:	Permeate volume (L)
ΔV_{FS}:	Change in the feed solution volume during the performance test (L)

References

[1] V.H. Tran, S. Lim, D.S. Han, N. Pathak, N. Akther, S. Phuntsho, H. Park, H.K. Shon, Efficient fouling control using outer-selective hollow fiber thin-film composite membranes for osmotic membrane bioreactor applications, Bioresource Technology, 282 (2019) 9-17.
[2] N. Akther, S. Daer, S.W. Hasan, Effect of flow rate, draw solution concentration and temperature on the performance of TFC FO membrane, and the potential use of RO reject brine as a draw solution in FO–RO hybrid systems, Desalination and Water Treatment, 136 (2018) 65-71.
[3] J. Zhang, Q. She, V.W.C. Chang, C.Y. Tang, R.D. Webster, Mining nutrients (N, K, P) from urban source-separated urine by forward osmosis dewatering, Environmental Science & Technology, 48 (2014) 3386-3394.
[4] V. Sant'Anna, L.D.F. Marczak, I.C. Tessaro, Membrane concentration of liquid foods by forward osmosis: Process and quality view, Journal of Food Engineering, 111 (2012) 483-489.
[5] N. Akther, S. Daer, Q. Wei, I. Janajreh, S.W. Hasan, Synthesis of polybenzimidazole (PBI) forward osmosis (FO) membrane and computational fluid dynamics (CFD) modeling of concentration gradient across membrane surface, Desalination, 452 (2019) 17-28.
[6] N. Akther, A. Sodiq, A. Giwa, S. Daer, H.A. Arafat, S.W. Hasan, Recent advancements in forward osmosis desalination: A review, Chemical Engineering Journal, 281 (2015) 502-522.
[7] A. Tiraferri, C.D. Vecitis, M. Elimelech, Covalent binding of single-walled carbon nanotubes to polyamide membranes for antimicrobial surface properties, ACS Applied Materials & Interfaces, 3 (2011) 2869-2877.
[8] A. Giwa, N. Akther, V. Dufour, S.W. Hasan, A critical review on recent polymeric and nano-enhanced membranes for reverse osmosis, RSC Advances, 6 (2016) 8134-8163.
[9] S. Lim, V.H. Tran, N. Akther, S. Phuntsho, H.K. Shon, Defect-free outer-selective hollow fiber thin-film composite membranes for forward osmosis applications, Journal of Membrane Science, 586 (2019) 281-291.
[10] Q.V. Ly, Y. Hu, J. Li, J. Cho, J. Hur, Characteristics and influencing factors of organic fouling in forward osmosis operation for wastewater applications: A comprehensive review, Environment International, 129 (2019) 164-184.
[11] M. Liu, S. Yu, J. Tao, C. Gao, Preparation, structure characteristics and separation properties of thin-film composite polyamide-urethane seawater reverse osmosis membrane, Journal of Membrane Science, 325 (2008) 947-956.
[12] R. Reis, L.F. Dumée, B.L. Tardy, R. Dagastine, J.D. Orbell, J.A. Schutz, M.C. Duke, Towards enhanced performance thin-film composite membranes via surface plasma modification, Scientific Reports, 6 (2016) 29206.
[13] C.Y. Tang, Y.-N. Kwon, J.O. Leckie, Effect of membrane chemistry and coating layer on physiochemical properties of thin film composite polyamide RO and NF membranes: II. Membrane physiochemical properties and their dependence on polyamide and coating layers, Desalination, 242 (2009) 168-182.
[14] Q.J. Niu, Reverse osmosis membrane with branched poly (alkylene oxide) modified antifouling surface, in, Google Patents, 2007.
[15] G. Kang, M. Liu, B. Lin, Y. Cao, Q. Yuan, A novel method of surface modification on thin-film composite reverse osmosis membrane by grafting poly(ethylene glycol), Polymer, 48 (2007) 1165-1170.
[16] N. Akther, S. Lim, V.H. Tran, S. Phuntsho, Y. Yang, T.-H. Bae, N. Ghaffour, H.K. Shon, The effect of Schiff base network on the separation performance of thin film nanocomposite forward osmosis membranes, Separation and Purification Technology, 217 (2019) 284-293.
[17] S. Lim, N. Akther, V.H. Tran, T.-H. Bae, S. Phuntsho, A. Merenda, L.F. Dumée, H.K. Shon, Covalent organic framework incorporated outer-selective hollow fiber thin-film

nanocomposite membranes for osmotically driven desalination, Desalination, 485 (2020) 114461.
[18] Q. Shen, Y. Lin, Y. Kawabata, Y. Jia, P. Zhang, N. Akther, K. Guan, T. Yoshioka, H. Shon, H. Matsuyama, Engineering heterostructured thin-film nanocomposite membrane with functionalized graphene oxide quantum dots (GOQD) for highly-efficient reverse osmosis, ACS Applied Materials & Interfaces, 12 (2020) 38662-38673.
[19] G. Zhao, R. Hu, Y. He, H. Zhu, Physically coating nanofiltration membranes with graphene oxide quantum dots for simultaneously improved water permeability and salt/dye rejection, Advanced Materials Interfaces, 6 (2019) 1801742.
[20] X. Song, L. Wang, C.Y. Tang, Z. Wang, C. Gao, Fabrication of carbon nanotubes incorporated double-skinned thin film nanocomposite membranes for enhanced separation performance and antifouling capability in forward osmosis process, Desalination, 369 (2015) 1-9.
[21] M. Ghanbari, D. Emadzadeh, W.J. Lau, T. Matsuura, A.F. Ismail, Synthesis and characterization of novel thin film nanocomposite reverse osmosis membranes with improved organic fouling properties for water desalination, RSC Advances, 5 (2015) 21268-21276.
[22] N. Akther, Z. Yuan, Y. Chen, S. Lim, S. Phuntsho, N. Ghaffour, H. Matsuyama, H. Shon, Influence of graphene oxide lateral size on the properties and performances of forward osmosis membrane, Desalination, 484 (2020) 114421.
[23] S. Lim, K.H. Park, V.H. Tran, N. Akther, S. Phuntsho, J.Y. Choi, H.K. Shon, Size-controlled graphene oxide for highly permeable and fouling-resistant outer-selective hollow fiber thin-film composite membranes for forward osmosis, Journal of Membrane Science, (2020) 118171.
[24] N. Akther, V. Sanahuja-Embuena, R. Górecki, S. Phuntsho, C. Helix-Nielsen, H.K. Shon, Employing the synergistic effect between aquaporin nanostructures and graphene oxide for enhanced separation performance of thin-film nanocomposite forward osmosis membranes, Desalination, 498 (2021) 114795.
[25] S.Y. Lee, H.J. Kim, R. Patel, S.J. Im, J.H. Kim, B.R. Min, Silver nanoparticles immobilized on thin film composite polyamide membrane: characterization, nanofiltration, antifouling properties, Polymers for Advanced Technologies, 18 (2007) 562-568.
[26] N. Akther, S. Phuntsho, Y. Chen, N. Ghaffour, H.K. Shon, Recent advances in nanomaterial-modified polyamide thin-film composite membranes for forward osmosis processes, Journal of Membrane Science, 584 (2019) 20-45.
[27] H.M. Hegab, A. ElMekawy, T.G. Barclay, A. Michelmore, L. Zou, C.P. Saint, M. Ginic-Markovic, Fine-tuning the surface of forward osmosis membranes via grafting graphene oxide: Performance patterns and biofouling propensity, ACS Applied Materials & Interfaces, 7 (2015) 18004-18016.
[28] H. Jin, F. Rivers, H. Yin, T. Lai, P. Cay-Durgun, A. Khosravi, M.L. Lind, P. Yu, Synthesis of AgCl mineralized thin film composite polyamide membranes to enhance performance and antifouling properties in forward osmosis, Industrial & Engineering Chemistry Research, 56 (2017) 1064-1073.
[29] J. Nikkola, J. Sievänen, M. Raulio, J. Wei, J. Vuorinen, C.Y. Tang, Surface modification of thin film composite polyamide membrane using atomic layer deposition method, Journal of Membrane Science, 450 (2014) 174-180.
[30] A. Soroush, W. Ma, M. Cyr, M.S. Rahaman, B. Asadishad, N. Tufenkji, In situ silver decoration on graphene oxide-treated thin film composite forward osmosis membranes: Biocidal properties and regeneration potential, Environmental Science & Technology Letters, 3 (2016) 13-18.
[31] T. Jin, Y. Ma, W. Matsuda, Y. Masuda, M. Nakajima, K. Ninomiya, T. Hiraoka, J.-y. Fukunaga, Y. Daiko, T. Yazawa, Preparation of surface-modified mesoporous silica

membranes and separation mechanism of their pervaporation properties, Desalination, 280 (2011) 139-145.
[32] V. Vatanpour, M. Kavian, Synergistic effect of silica nanoparticles in the matrix of a poly(ethylene glycol) diacrylate coating layer for the surface modification of polyamide nanofiltration membranes, Journal of Applied Polymer Science, 133 (2016).
[33] Z. Wang, X. Jiang, X. Cheng, C.H. Lau, L. Shao, Mussel-inspired hybrid coatings that transform membrane hydrophobicity into high hydrophilicity and underwater superoleophobicity for oil-in-water emulsion separation, ACS Applied Materials & Interfaces, 7 (2015) 9534-9545.
[34] L. Xing, N. Guo, Y. Zhang, H. Zhang, J. Liu, A negatively charged loose nanofiltration membrane by blending with poly (sodium 4-styrene sulfonate) grafted SiO2 via SI-ATRP for dye purification, Separation and Purification Technology, 146 (2015) 50-59.
[35] L. Zhang, Y. Lin, H. Wu, L. Cheng, Y. Sun, T. Yasui, Z. Yang, S. Wang, T. Yoshioka, H. Matsuyama, An ultrathin in situ silicification layer developed by an electrostatic attraction force strategy for ultrahigh-performance oil–water emulsion separation, Journal of Materials Chemistry A, 7 (2019) 24569-24582.
[36] S. Daer, N. Akther, Q. Wei, H.K. Shon, S.W. Hasan, Influence of silica nanoparticles on the desalination performance of forward osmosis polybenzimidazole membranes, Desalination, 491 (2020) 114441.
[37] K. Huang, X. Quan, X. Li, F.H. Tezel, B. Li, Improved surface hydrophilicity and antifouling property of nanofiltration membrane by grafting NH2-functionalized silica nanoparticles, Polymers for Advanced Technologies, 29 (2018) 3159-3170.
[38] N. Akther, S.M. Ali, S. Phuntsho, H. Shon, Surface modification of thin-film composite forward osmosis membranes with polyvinyl alcohol–graphene oxide composite hydrogels for antifouling properties, Desalination, 491 (2020) 114591.
[39] S. Romero-Vargas Castrillón, X. Lu, D.L. Shaffer, M. Elimelech, Amine enrichment and poly(ethylene glycol) (PEG) surface modification of thin-film composite forward osmosis membranes for organic fouling control, Journal of Membrane Science, 450 (2014) 331-339.
[40] S. Lee, C. Boo, M. Elimelech, S. Hong, Comparison of fouling behavior in forward osmosis (FO) and reverse osmosis (RO), Journal of Membrane Science, 365 (2010) 34-39.
[41] B. Scheibe, E. Borowiak-Palen, R. Kalenczuk, Effect of the silanization processes on the properties of oxidized multiwalled carbon nanotubes, Acta Physica Polonica, A., 116 (2009).
[42] C.C.M.C. Carcouët, M.W.P. van de Put, B. Mezari, P.C.M.M. Magusin, J. Laven, P.H.H. Bomans, H. Friedrich, A.C.C. Esteves, N.A.J.M. Sommerdijk, R.A.T.M. van Benthem, G. de With, Nucleation and growth of monodisperse silica nanoparticles, Nano Letters, 14 (2014) 1433-1438.
[43] D.J. Belton, O. Deschaume, C.C. Perry, An overview of the fundamentals of the chemistry of silica with relevance to biosilicification and technological advances, FEBS Journal, 279 (2012) 1710-1720.
[44] G.S. Lai, W.J. Lau, P.S. Goh, A.F. Ismail, Y.H. Tan, C.Y. Chong, R. Krause-Rehberg, S. Awad, Tailor-made thin film nanocomposite membrane incorporated with graphene oxide using novel interfacial polymerization technique for enhanced water separation, Chemical Engineering Journal, 344 (2018) 524-534.
[45] C.Y. Tang, Y.-N. Kwon, J.O. Leckie, Effect of membrane chemistry and coating layer on physiochemical properties of thin film composite polyamide RO and NF membranes: I. FTIR and XPS characterization of polyamide and coating layer chemistry, Desalination, 242 (2009) 149-167.
[46] G. De, B. Karmakar, D. Ganguli, Hydrolysis–condensation reactions of TEOS in the presence of acetic acid leading to the generation of glass-like silica microspheres in solution at room temperature, Journal of Materials Chemistry, 10 (2000) 2289-2293.

[47] K.-M. Li, J.-G. Jiang, S.-C. Tian, X.-J. Chen, F. Yan, Influence of silica types on synthesis and performance of amine–silica hybrid materials used for CO2 capture, The Journal of Physical Chemistry C, 118 (2014) 2454-2462.
[48] S. Sánchez, M. Pumera, E. Fàbregas, J. Bartrolí, M.J. Esplandiu, Carbon nanotube/polysulfone soft composites: Preparation, characterization and application for electrochemical sensing of biomarkers, Physical Chemistry Chemical Physics, 11 (2009) 7721-7728.
[49] B. Hu, L. Liu, Y. Zhao, C. Lü, A facile construction of quaternized polymer brush-grafted graphene modified polysulfone based composite anion exchange membranes with enhanced performance, RSC Advances, 6 (2016) 51057-51067.
[50] H. Hafeez, D.K. Choi, C.M. Lee, P.J. Jesuraj, D.H. Kim, A. Song, K.B. Chung, M. Song, J.F. Ma, C.-S. Kim, S.Y. Ryu, Replacement of n-type layers with a non-toxic APTES interfacial layer to improve the performance of amorphous Si thin-film solar cells, RSC Advances, 9 (2019) 7536-7542.
[51] W.J. Lau, A.F. Ismail, P.S. Goh, N. Hilal, B.S. Ooi, Characterization methods of thin film composite nanofiltration membranes, Separation & Purification Reviews, 44 (2015) 135-156.
[52] H.-C. Yang, J.-K. Pi, K.-J. Liao, H. Huang, Q.-Y. Wu, X.-J. Huang, Z.-K. Xu, Silica-decorated polypropylene microfiltration membranes with a mussel-inspired intermediate layer for oil-in-water emulsion separation, ACS Applied Materials & Interfaces, 6 (2014) 12566-12572.
[53] M. Liu, Q. Chen, L. Wang, S. Yu, C. Gao, Improving fouling resistance and chlorine stability of aromatic polyamide thin-film composite RO membrane by surface grafting of polyvinyl alcohol (PVA), Desalination, 367 (2015) 11-20.
[54] L.M. Jin, S.L. Yu, W.X. Shi, X.S. Yi, N. Sun, Y.L. Ge, C. Ma, Synthesis of a novel composite nanofiltration membrane incorporated SiO2 nanoparticles for oily wastewater desalination, Polymer, 53 (2012) 5295-5303.
[55] B. Mi, M. Elimelech, Chemical and physical aspects of organic fouling of forward osmosis membranes, Journal of Membrane Science, 320 (2008) 292-302.
[56] Y. Mo, A. Tiraferri, N.Y. Yip, A. Adout, X. Huang, M. Elimelech, Improved antifouling properties of polyamide nanofiltration membranes by reducing the density of surface carboxyl groups, Environmental Science & Technology, 46 (2012) 13253-13261.
[57] M. Rastgar, A. Shakeri, A. Bozorg, H. Salehi, V. Saadattalab, Highly-efficient forward osmosis membrane tailored by magnetically responsive graphene oxide/Fe3O4 nanohybrid, Applied Surface Science, 441 (2018) 923-935.